FOUNDATIONS

ADVANCES

Supporting information for article:

Complex structural ordering of the oxygen deficiency in La$_{0.5}$Ca$_{2.5}$Mn$_2$O$_{7-\delta}$ Ruddlesden–Popper phases

Daniel González-Merchante, Raquel Cortés-Gil, José M. Alonso, Emilio Matesanz, José L. Martínez, Alberto Rivera-Calzada, Jacobo Santamaría, M. Luisa Ruiz-González and José M. González-Calbet

S1. Oxygen vacancy arrangements for the structural model corresponding to the n=2 Ruddlesden-Popper (RP) term $A_3B_2O_7$

In the case of reduced $A_3B_2O_{7-\delta}$, two oxygen vacancy arrangements have been described for different compositions: vacancies located in the middle of the double perovskite (P) layers (apical oxygen) and vacancies located in the equatorial sites (equatorial oxygen) that means in the BO_2 planes. In both cases, square-pyramids polyhedra are formed and could give rise to new ordered superlattices.
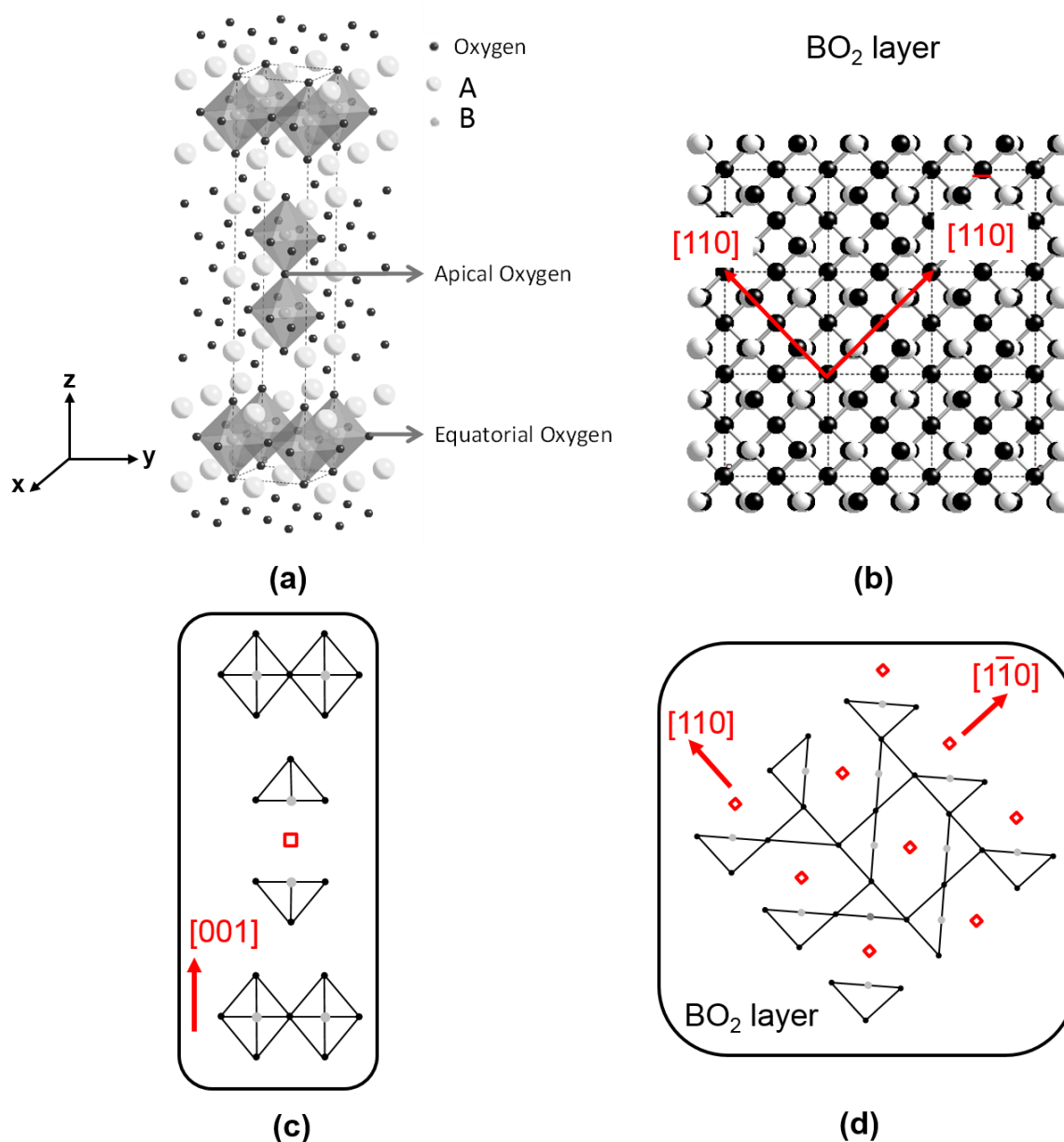

Figure S1 (a) Structural model corresponding to the n=2 Ruddlesden-Popper term $A_3B_2O_7$. Notice the two kinds of oxygen sites: the equatorial and the apical one; (b) The BO_2 layer as well as the [110] and [1-10] direction. (c) Schematic pattern of the ordering of the anionic vacancies along [001] direction due to the removal of some apical oxygens (d) Schematic pattern of the ordering of the anionic vacancies in the BO_2 layer. A superlattice along [110] and [1-10] direction is formed.

S2. Thermogravimetric curves corresponding to the reduction processes La$_{0.5}$Ca$_{2.5}$Mn$_2$O$_7$ → La$_{0.5}$Ca$_{2.5}$Mn$_2$O$_{6.5}$ and La$_{0.5}$Ca$_{2.5}$Mn$_2$O$_7$ → La$_{0.5}$Ca$_{2.5}$Mn$_2$O$_{6.25}$

The experimental conditions to synthesize La$_{0.5}$Ca$_{2.5}$Mn$_2$O$_{6.5}$ and La$_{0.5}$Ca$_{2.5}$Mn$_2$O$_{6.25}$ have been described in the main text (Experimental section). The corresponding thermogravimetric curves are shown in figure S2.
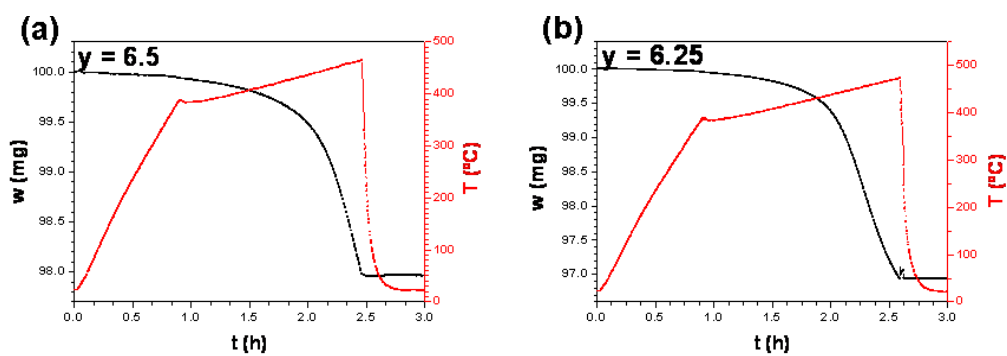

Figure S2 Thermogravimetric curves corresponding to the synthesis of (a) La$_{0.5}$Ca$_{2.5}$Mn$_2$O$_{6.5}$ and (b) La$_{0.5}$Ca$_{2.5}$Mn$_2$O$_{6.25}$.

S3. XRD patterns corresponding to La$_{0.5}$Ca$_{2.5}$Mn$_2$O$_{7-\sigma}$ (σ=0, 0.5 and 0.75)

The X-Ray diffraction (XRD) pattern corresponding to the starting material can be indexed on the basis of an orthorhombic (Cmc2$_1$) RP n=2 term with parameters a=1.93157(2) nm, b=0.53682(1) nm and c=0.53403(1) nm (figure S3a). The XRD patterns corresponding to the reduced samples (figure S3b and c) are quite similar, suggesting a topotactic reducing process. Notice the appearance of the (200) reflection (d$_{hkl}$= 0.95 nm) in the three patterns characteristic of the n=2 RP member. Nevertheless, slight different features can be observed, as the splitting of the (020) reflection as well as the shifting of the ($\underline{10}$ 0 0) and (312) reflections towards lower 2θ value as indicated in the inset of figure S3. These facts indicate that even when the basic structural skeleton is kept additional structural features, probably related to an increase of the orthorhombic distortion, are present. It is worth recalling that the models of oxygen vacancies described above, apical and equatorial, were tested for fitting the experimental XRD data. All the attempts using different tetragonal and orthorhombic symmetry failed, since significant differences between the model and experimental data were always found for the reduced samples, indicating a more complex reduction process. In order to get more complete structural information and elucidate whether or not short range order-disorder phenomena appear, quite frequent on RP high members, an exhaustive transmission electron microscopy characterization was performed.
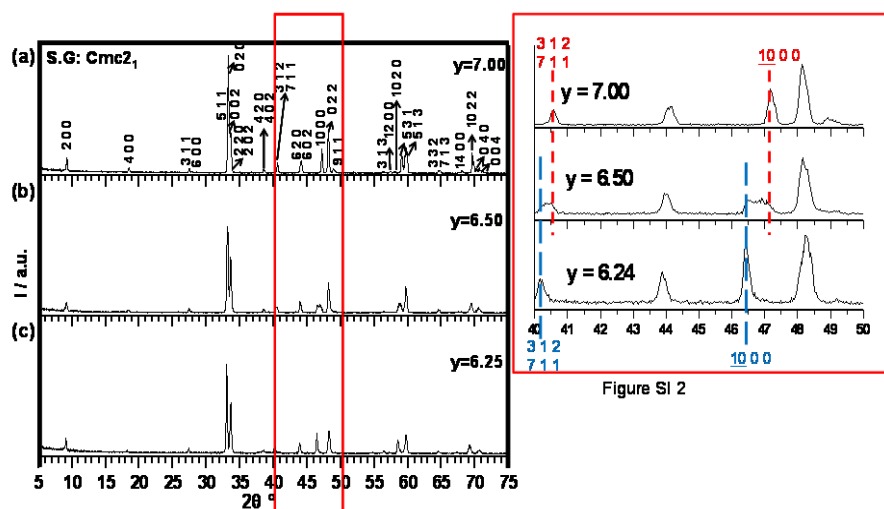

Figure S3 XRD patterns corresponding to (a) La$_{0.5}$Ca$_{2.5}$Mn$_2$O$_7$, (b) La$_{0.5}$Ca$_{2.5}$Mn$_2$O$_{6.5}$ and (c) La$_{0.5}$Ca$_{2.5}$Mn$_2$O$_{6.25}$.

S4. Chemical analysis determination by EPMA and EDS

Cation compositional analysis has been determined by means of electron microprobe microanalysis (EPMA), attached to a JEOL JXA-8900 microscope analyzing around 20 areas of 1-5 µm. Experimental results corresponding to the starting material are shown in table S1 leading to the average $La_{0.56}Ca_{2.43}Mn_{2.01}O_y$ composition per unit formula. A nice fit with the nominal composition is obtained.

	Mn	La	Ca
1	18.0635	5.5184	20.7103
2	17.2767	4.7832	20.9053
3	17.1349	4.6230	20.8293
4	16.8604	4.5224	20.7663
5	17.2352	4.8294	20.8645
6	16.5289	4.5461	20.3499
7	17.2309	4.4141	20.8799
8	16.8836	4.8626	20.1439
9	16.8894	4.6645	20.5697
10	16.5532	4.6223	19.9914
Average	17.0657 (**±0.15**)	4.7386 (**±0.15**)	20.6010 (**±0.15**)

Table S1   Atomic percentages (%) obtained on 10 representative areas of the starting sample.

In addition, a more local study has been performed in individual crystals by means of EDS in JEOL JEM 2100 microscope fitted with an Oxford INCA spectrometer. A total of 20 particles were analyzed leading to the $La_{0.57\pm0.1}Ca_{2.47\pm0.1}Mn_{1.93\pm0.1}O_y$ average composition, in agreement to the nominal one.

S5. Transmission Electron Microscopy
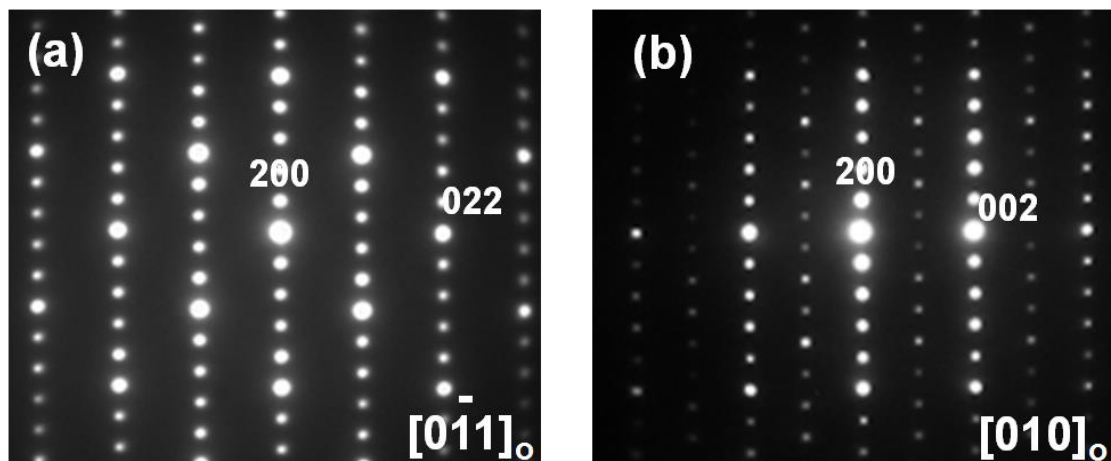
S5.1. SAED along [0-11] and [010]

Figure S4 SAED patterns corresponding to $La_{0.5}Ca_{2.5}Mn_2O_{6.25}$ along (a) $[0\bar{1}1]_o$ and (b) $[010]$ zone axes.

S5.2. Additional reflections in SAED along [100]

It is worth emphasizing the difficulty to stabilize high ordered pure terms of RP phases, which are frequently obtained as disordered intergrowths between the basic unities, unless a controlled layer by layer physical method is used (Rijnders, 2014; Lee *et al.,* 2014; Yan *et al.,* 2007). In this sense, we have recently (Ruiz-González *et al.,*2015) reported the stabilization of the $La_{0.5}Ca_{2.5}Mn_2O_7$ containing micrometric crystalline particles with a well ordered distribution of two P and one RS as shown for $La_{0.5}Ca_{2.5}Mn_2O_{6.5}$ (figure 1c). Nevertheless, this apparently long range structural order was linked to unconventional short range order-disorder phenomena of La and Ca cations, studied with atomic resolution techniques. A sites in the RS blocks are occupied by Ca whereas this position in the P layer shows a mixed La and Ca occupancy.

Apart from this description, it should be noticed that other authors have proposed a 2D incommensurate modulation in $La_{2-2x}Ca_{1+2x}Mn_2O_7$ normal to the b axis, since additional satellite reflections appear around the fundamental spots in the basal projection of the electron diffraction. (Bendersky *et al*., 2004). Such extra spots have been subject of discussion leading to different approaches such as their relation to a plausible charge ordering (CO) state between Mn^{4+} and Mn^{3+}, or chemical ordering between Ca and La. According to our previous EELS (Electron Energy Loss Spectroscopy) atomic resolved studies (Ruiz-González *et al.,* 2015) in $La_{0.5}Ca_{2.5}Mn_2O_7$, Mn^{3+} and Mn^{4+} are mainly, at room temperature, randomly distributed. On the other hand, in our case, the La

and Ca atomically resolved distribution does not justify the extra spot reported by L. A. Bendersky *et al*., (2004). In this scenario, it must be taken into account that the above authors indicate that $La_{2-2x}Ca_{1+2x}Mn_2O_7$ is slightly oxygen deficient. In our case, the oxygen sublattice is complete and no additional reflections are observed. Nevertheless, we have also ascertained that when the oxygen content is slightly reduced the additional spots also appear (Ruiz-González *et al.,* 2015). This result evidences that these extra spots are related to the accommodation of the oxygen vacancies.

Concerning the reduced samples, the observation of the diffuse character of the spots in the SAED pattern (figure 2) and the subtle superlattice visualized in the corresponding HRTEM (figure 3), suggests an order-disorder distribution of the non-occupied oxygen sites. The order should be associated to a strong tendency or preferential elimination of the oxygen atoms from those sites marked in figure 2c providing additional spots in the SAED pattern (figure 3) and the superlattice detected in the HRTEM image (figure 2). Notice that the elimination of one oxygen atom every second one along the $[031]_o$ and $[0\bar{1}3]_o$ perpendicular directions in each MnO_2 layer, along [100], of the original n=2 RP phase would lead to an oxygen content of 6.6 atoms per unit cell. The oxygen content of the reduced samples here prepared are 6.5 and 6.25, meaning (especially for the $O_{6.25}$ sample) that the oxygen content is even lower, therefore, more oxygen sites should be removed. Nevertheless, since the oxygen content of the sample is lower, additional oxygen atoms should be randomly removed from their sites. This would lead to disorder, justifying the diffuse character of the spots and periodicities in the SAED pattern and HRTEM image, respectively.

S6. Neutron Diffraction Refinement

The refinement was done considering the following constraints related to the composition: the nominal composition $La_{0.5}Ca_{2.5}Mn_2O_{6.25}$, according to EDS and thermogravimetric studies, was considered being La always at the twelve coordination of the P block while Ca occupies both the P and RS sites, according to the atomically resolved HAADF and EELS mapping study (see figure S8). On the other hand, constrains were also applied to refined O occupation factors to be kept between 0 and 1 during the refinement process. Following a similar methodology that the one reported in previous works, (Gillie *et al*., 2002; Gillie *et al*., 2003) we have started considering the complete anionic sublattice, modifying the oxygen occupancy of the oxygen sites marked in figure 3c. But, since this model renders $O_{6.6}$ content, a partial occupancy of other O sites of the MnO_2 layers have been taken into account. Over the structural refinement, different occupation factors of the oxygen sites were tested constraining the total oxygen composition to the nominal value $O_{6.25}$, leading to partially oxygen occupied positions in the MnO_2 plane. These findings resemble the structures published for related phases and support the diffuse nature of the SAED additional reflections together with the poor contrast observed in the HRTEM image for the superstructure. In order to end up with an acceptable final structure, soft constrains were applied on Ca-O, Ca/La-O and Mn-O distances. On the other hand, it is worth mentioning that being impossible to refine individual thermal parameters for every atom in the structure, an overall thermal factor was refined instead. Figure S5 shows the final refinement of the ND pattern. Starting model for refinement as derived from the ordered pattern of anionic vacancies is depicted in figure S6a-d. The final structural parameters resulting from the refinement are collected in table S2, and the corresponding interatomic selected distances and bond angles are gathered in table S3.
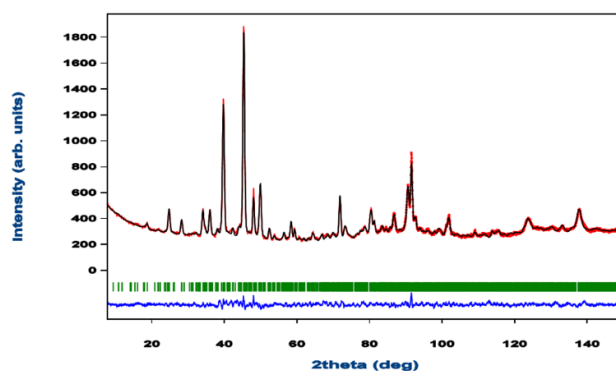
Figure S5 ND pattern (red points) and Rietveld fit (black line) of $La_{0.5}Ca_{2.5}Mn_2O_{6.25}$ at room temperature. The difference between experimental and calculated data is shown as a solid line in blue. The parameters of the monoclinic unit cell are: a_m=0.84186(4) nm, b_m=1.95707(4) nm, c_m=0.84680(4) nm, β=89.983(4). Vertical bars show all allowed reflections of the SG P2/m (R_{wp}=3.01, R_p=2.32 and χ^2=3.0).
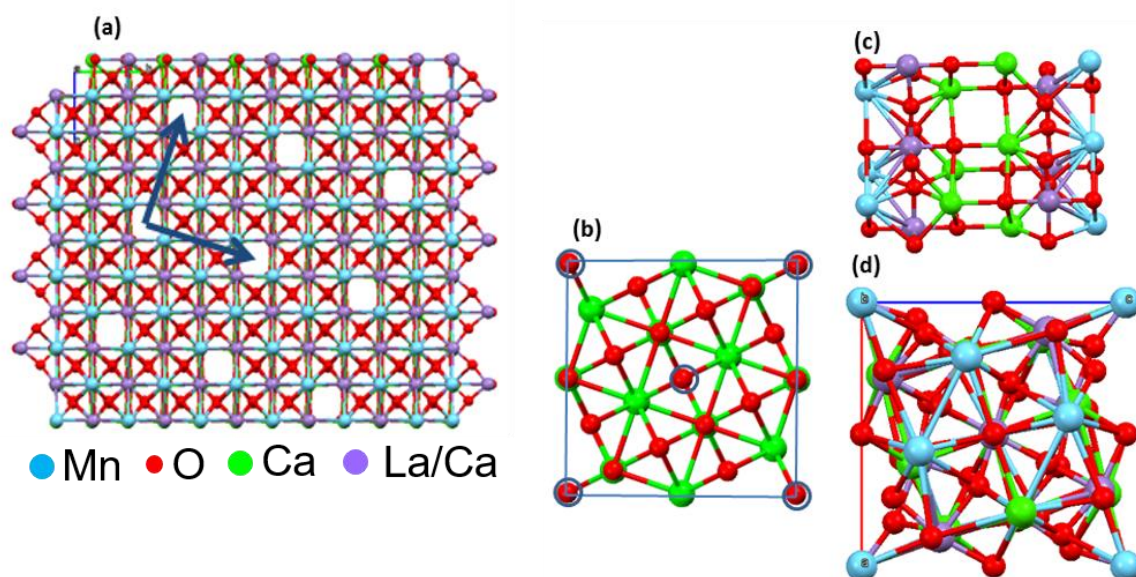
Figure S6 (a) Original model (Cmc2$_1$) for the vacancy ordering; the blue arrows show the [031]$_o$ and [0$\bar{1}$3]$_o$ directions where the oxygen positions should be empty according to the starting atomic model; (b) new triclinic unit cell (a=1.96 nm; b=c=0.86 nm; α=β=γ=90º) along the [100]$_o$ zone axis. This unit cell is based on the less distorted Sr$_3$Mn$_2$O$_7$ (structure type Sr$_3$Ti$_2$O$_7$, tetragonal I4/mmm) unit cell. Two different orientations have been considered to finally get this triclinic unit cell. First, to get this symmetry, an orthorhombic (o´) one was derived from the tetragonal through a rotation of 45º in the plane, leading to parameters: a$_o$´= b$_o$´ = a$_t\sqrt{2}$; c$_o$´ = c$_t$. Second, the change associated to the new superstructure involves a 18.44º rotation in the plane, leading to the new parameters: c$_n$=c$_o$´=0.199 nm ; a$_n=\sqrt{[(3/2\ a_{o'})^2 + (1/2\ b_{o'})^2]}$=0.85 nm and b$_n=\sqrt{[(1/2\ a_{o'})^2 + (3/2\ b_{o'})^2]}$=0.85 nm. The red atoms marked with blue circles indicate the oxygen atomic columns which should be removed to generate a new superstructure; (c) new asymmetric unit cell generated by FINDsym software. (d) Final monoclinic P2/m unit cell (m) used as starting point of the Rietveld structure refinement of the neutron diffraction pattern.

Table S2   Refined Atomic Parameters of $La_{0.5}Ca_{2.5}Mn_2O_{6.25}$.

Atom Label	Atom Type	x	y	z	occ
Ca21	Ca	0.133(3)	0.1860(20)	0.678(4)	1
Ca22	Ca	0.276(3)	0.1837(18)	0.075(4)	1
Ca23	Ca	0.5	0.179(2)	0.5	1
Ca24	Ca	0.0	0.316(3)	0.0	1
Ca25	Ca	0.198(4)	0.3139(18)	0.395(3)	1
Ca26	Ca	0.388(4)	0.3141(17)	0.810(4)	1
Ca11	Ca	0.133(4)	0.0	0.688(4)	0.5
Ca12	Ca	0.291(4)	0.0	0.089(4)	0.5
Ca13	Ca	0.5	0.0	0.5	0.5
Ca14	Ca	0.0	0.5	0.0	0.5
Ca15	Ca	0.207(4)	0.5	0.397(4)	0.5
Ca16	Ca	0.436(4)	0.5	0.783(4)	0.5
La11	La	0.133(4)	0.0	0.688(4)	0.5
La12	La	0.291(4)	0.0	0.089(4)	0.5
La13	La	0.5	0.0	0.5	0.5
La14	La	0.0	0.5	0.0	0.5
La15	La	0.207(4)	0.5	0.397(4)	0.5
La16	La	0.436(4)	0.5	0.783(4)	0.5
Mn11	Mn	0.0	0.0972(16)	0.0	1
Mn12	Mn	0.201(3)	0.0943(14)	0.402(3)	1
Mn13	Mn	0.399(3)	0.0999(14)	0.789(3)	1
Mn14	Mn	0.111(3)	0.4029(14)	0.706(3)	1
Mn15	Mn	0.284(3)	0.4009(14)	0.099(3)	1
Mn16	Mn	0.5	0.4017(16)	0.5	1
O101	O	0.0	0.0	0.0	1
O102	O	0.189(4)	0.0	0.332(3)	1
O103	O	0.441(4)	0.0	0.821(4)	1
O104	O	0.108(5)	0.5	0.737(4)	1

O105	O	0.257(4)	0.5	0.087(4)	1
O106	O	0.5	0.5	0.5	1
O201	O	0.0	0.1955(18)	0.0	1
O202	O	0.174(3)	0.1930(13)	0.413(3)	1
O203	O	0.409(3)	0.1985(11)	0.852(3)	1
O204	O	0.105(3)	0.3013(12)	0.707(3)	1
O205	O	0.306(3)	0.3050(13)	0.101(3)	1
O206	O	0.5	0.3024(16)	0.5	1
O301	O	0.0	0.0874(18)	0.5	1
O302	O	0.064(5)	0.099(3)	0.208(4)	0.56(5)
O303	O	0.166(3)	0.093(2)	0.877(3)	0.71(6)
O304	O	0.333(2)	0.0971(17)	0.590(3)	1
O305	O	0.379(3)	0.0958(17)	0.255(3)	1
O306	O	0.5	0.088(3)	0.0	0.58(8)
O307	O	0.0	0.401(8)	0.5	0.24(8)
O308	O	0.120(3)	0.4062(19)	0.241(3)	0.74(5)
O309	O	0.261(2)	0.4056(17)	0.882(2)	1
O310	O	0.304(2)	0.4061(17)	0.560(3)	1
O311	O	0.391(4)	0.401(2)	0.297(3)	0.71(6)
O312	O	0.5	0.4000(19)	0.0	1

Table S3   Distances and angles around selected atom sites

Atom site		Distance (nm)		Angle (°)
Mn11	(Mn11)-(O101)	0.190(3)	(O101)-(Mn11)-(O201)	180(3)
	(Mn11)-(O201)	0.192(5)	(O302)-(Mn11)-(O302)	178(3)
	(Mn11)-(O302)	0.184(3)	(O303)-(Mn11)-(O303)	175(3)
	(Mn11)-(O303)	0.174(3)	(O101)-(Mn11)-(O302)	91(3)
			(O201)-(Mn11)-(O302)	89(3)
			(O101)-(Mn11)-(O303)	87.3(19)
			(O201)-(Mn11)-(O303)	93(3)
			(O302)-(Mn11)-(O303)	110(3)
			(O302)-(Mn11)-(O303)	70(2)
Mn12	(Mn12)-(O102)	0.194(3)	(O102)-(Mn12)-(O202)	162(2)
	(Mn12)-(O202)	0.195(4)	(O301)-(Mn12)-(O305)	166.0(20)
	(Mn12)-(O301)	0.189(3)	(O302)-(Mn12)-(O304)	176(3)
	(Mn12)-(O302)	0.201(4)	(O102)-(Mn12)-(O301)	91.1(18)
	(Mn12)-(O304)	0.194(3)	(O102)-(Mn12)-(O302)	76(2)
	(Mn12)-(O305)	0.195(4)	(O102)-(Mn12)-(O304)	108(2)
			(O102)-(Mn12)-(O305)	81.9(20)
			(O202)-(Mn12)-(O301)	87(2)
			(O202)-(Mn12)-(O302)	86(3)
			(O202)-(Mn12)-(O304)	90(2)
			(O202)-(Mn12)-(O305)	96(2)
			(O301)-(Mn12)-(O302)	81.3(20)
			(O301)-(Mn12)-(O304)	98.9(15)
			(O302)-(Mn12)-(O305)	85(3)
			(O304)-(Mn12)-(O305)	95(2)

Mn13	(Mn13)-(O103)	0.201(3)	(O103)-(Mn13)-(O203)	153.6(18)
	(Mn13)-(O203)	0.200(3)	(O303)-(Mn13)-(O305)	169(3)
	(Mn13)-(O303)	0.210(4)	(O304)-(Mn13)-(O306)	169(2)
	(Mn13)-(O304)	0.178(4)	(O103)-(Mn13)-(O303)	93(2)
	(Mn13)-(O305)	0.191(4)	(O103)-(Mn13)-(O304)	99(2)
	(Mn13)-(O306)	0.199(3)	(O103)-(Mn13)-(O305)	79.2(19)
			(O103)-(Mn13)-(O306)	71.9(20)
			(O203)-(Mn13)-(O303)	90(2)
			(O203)-(Mn13)-(O304)	107(2)
			(O203)-(Mn13)-(O305)	93(2)
			(O203)-(Mn13)-(O306)	82(2)
			(O303)-(Mn13)-(O304)	92(2)
			(O303)-(Mn13)-(O306)	94.2(16)
			(O304)-(Mn13)-(O305)	97(2)
			(O305)-(Mn13)-(O306)	75.6(16)
Mn14	(Mn14)-(O104)	0.192(3)	(O104)-(Mn14)-(O204)	171.6(19)
	(Mn14)-(O204)	0.199(4)	(O307)-(Mn14)-(O309)	167.9(15)
	(Mn14)-(O307)	0.198(3)	(O308)-(Mn14)-(O310)	155(2)
	(Mn14)-(O308)	0.200(4)	(O104)-(Mn14)-(O307)	98(5)
	(Mn14)-(O309)	0.195(3)	(O104)-(Mn14)-(O308)	86(2)
	(Mn14)-(O310)	0.204(3)	(O104)-(Mn14)-(O309)	83.0(19)
			(O104)-(Mn14)-(O310)	94(2)
			(O204)-(Mn14)-(O307)	88(5)
			(O204)-(Mn14)-(O308)	90(2)
			(O204)-(Mn14)-(O309)	92(2)
			(O204)-(Mn14)-(O310)	93(2)
			(O307)-(Mn14)-(O308)	74.9(16)
			(O307)-(Mn14)-(O310)	81.0(14)

			(O308)-(Mn14)-(O309)	117(2)
			(O309)-(Mn14)-(O310)	86.9(18)
Mn15	(Mn15)-(O105)	0.196(3)	(O105)-(Mn15)-(O205)	177(2)
	(Mn15)-(O205)	0.189(4)	(O308)-(Mn15)-(O312)	163(2)
	(Mn15)-(O308)	0.183(4)	(O309)-(Mn15)-(O311)	158(2)
	(Mn15)-(O309)	0.185(3)	(O105)-(Mn15)-(O308)	84(2)
	(Mn15)-(O311)	0.190(4)	(O105)-(Mn15)-(O309)	83.5(19)
	(Mn15)-(O312)	0.200(3)	(O105)-(Mn15)-(O311)	96(2)
			(O105)-(Mn15)-(O312)	95.3(19)
			(O205)-(Mn15)-(O308)	97(2)
			(O205)-(Mn15)-(O309)	94(2)
			(O205)-(Mn15)-(O311)	87(2)
			(O205)-(Mn15)-(O312)	84.6(20)
			(O308)-(Mn15)-(O309)	125(2)
			(O308)-(Mn15)-(O311)	77(2)
			(O309)-(Mn15)-(O312)	71.3(13)
			(O311)-(Mn15)-(O312)	86.5(17)
Mn16	(Mn16)-(O106)	0.192(3)	(O106)-(Mn16)-(O206)	180(2)
	(Mn16)-(O206)	0.194(4)	(O310)-(Mn16)-(O310)	174.3(19)
	(Mn16)-(O310)	0.1729(18)	(O311)-(Mn16)-(O311)	179(3)
	(Mn16)-(O311)	0.195(3)	(O106)-(Mn16)-(O310)	87.1(16)
			(O106)-(Mn16)-(O311)	90.4(19)
			(O206)-(Mn16)-(O310)	93(2)
			(O206)-(Mn16)-(O311)	90(2)
			(O310)-(Mn16)-(O311)	79.0(18)
			(O310)-(Mn16)-(O311)	101(2)

Atom site	Distance (nm)		Atom site	Distance (nm)	
Ca11/La11	(Ca11)-(O301)	0.259(3)	Ca21	(Ca21)-(O301)	0.269(4)
	(Ca11)-(O302)	0.270(6)		(Ca21)-(O302)	0.257(6)
	(Ca11)-(O303)	0.244(4)		(Ca21)-(O303)	0.250(5)
	(Ca11)-(O304)	0.267(4)		(Ca21)-(O304)	0.253(4)
Ca12/La12	(Ca12)-(O302)	0.290(6)	Ca22	(Ca22)-(O302)	0.268(6)
	(Ca12)-(O303)	0.276(4)		(Ca22)-(O303)	0.261(5)
	(Ca12)-(O305)	0.246(4)		(Ca22)-(O305)	0.246(4)
	(Ca12)-(O306)	0.257(5)		(Ca22)-(O306)	0.273(5)
Ca13/La13	(Ca13)-(O304)	0.248(3)	Ca23	(Ca23)-(O304)	0.226(4)
	(Ca13)-(O305)	0.298(3)		(Ca23)-(O304)	0.226(4)
				(Ca23)-(O305)	0.283(4)
				(Ca23)-(O305)	0.283(4)
Ca14/La14	(Ca14)-(O308)	0.293(3)			
	(Ca14)-(O309)	0.304(2)			
			Ca24	(Ca24)-(O308)	0.288(5)
				(Ca24)-(O309)	0.298(4)
Ca15/La15	(Ca15)-(O307)	0.275(11)			
	(Ca15)-(O308)	0.238(4)			
	(Ca15)-(O310)	0.244(4)	Ca25	(Ca25)-(O307)	0.254(11)
	(Ca15)-(O311)	0.262(4)		(Ca25)-(O308)	0.232(5)
				(Ca25)-(O310)	0.245(4)
				(Ca25)-(O311)	0.250(5)
Ca16/La16	(Ca16)-(O309)	0.251(4)			

(Ca16)-(O310)	0.286(4)			
(Ca16)-(O311)	0.252(4)	Ca26	(Ca26)-(O309)	0.217(4)
(Ca16)-(O312)	0.274(4)		(Ca26)-(O310)	0.287(4)
			(Ca26)-(O311)	0.268(5)
			(Ca26)-(O312)	0.251(4)

Figure S7 depicts the final refined unit cell showing the O occupancy. It should be noticed, according to the structural parameters displayed in table S2, that the highest octahedral deformation is related to that oxygen sites exhibiting the highest percentage of anionic vacancies, i.e., the equatorial positions marked in black in figure S7.
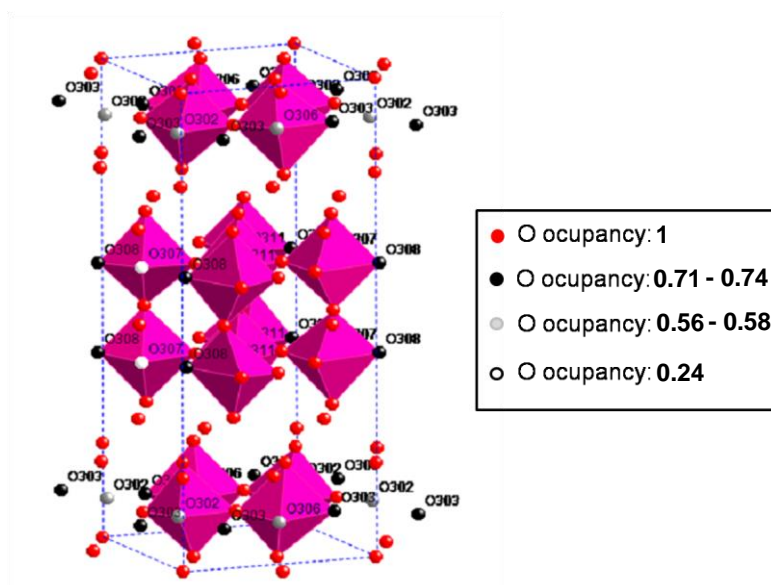
Figure S7 Structural model of $La_{0.5}Ca_{2.5}Mn_2O_{6.25}$. Only the oxygen atoms are shown for clearness. The different colors of the oxygen atoms correspond to changes in the occupancy as shown in the inset.

S7. Atomically resolved characterization

In order to get further structural and compositional information about the cation and anion distribution as well as the Mn oxidation state, an atomically resolved study was performed in an aberrated corrected Scanning Transmission Electron Microscope (STEM) JEOL JSM-ARM200cF microscope (Cold Emission Gun) using two different imaging techniques in STEM mode: HAADF (high annular angle dark field) and ABF (annular bright field). At the same time, a complete compositional analysis was performed through the acquisition of either EELS chemical maps (in order to determine the cation distribution) or EELS punctual spectra (for Mn oxidation state determination).

HAADF implies the collection of the electrons scattered at high angles (Solid semi-angles between 68-280 mrad) resulting in incoherent imaging. Under these experimental conditions, the scattered intensity is approximately proportional to $Z^{1.83}$ (Z=atomic number of the elements in the sample). In this sense, the intensity differences among columns must be related to the different cationic composition, i.e. La (Z=57), Ca (Z=20) and Mn (Z=25) in our case, and therefore, HAADF provides images which contrast can be qualitative interpreted as chemical information: the brighter contrast would correspond to heaviest elements while less bright contrast to those elements with lower Z. The incorporation of spherical aberration correctors allows acquiring HAADF images with atomic resolution, making possible to resolve and locate cationic columns with different atomic number. The microscope is equipped with a GIF-QuantumER^{TM} spectrometer used for acquisition of EELS maps with a spatial resolution ~0.04 nm, over a total acquisition time of ~2 min using 18 and 20.3 mrad convergence and collection semi-angles, respectively. Simultaneously, the zero loss peak was also acquired by using Dual EELS, meaning that the experimental signal is perfectly aligned and calibrated. Principal Component Analysis (Bonnet *et al.*, 1999) was performed on EELS data set to de-noise the spectra by using the Hyperspy data analysis toolbox (http://hyperspy.org; DOI 10.5281/zenodo.16850). Chemical maps were constructed selecting the elements to identify and considering the experimental conditions: beam energy (200 kV). A power-law background subtraction was used for the selected spectrum and all the edge setup applied to the parent spectrum imaging.[10] The relative thickness has been calculated from low loss spectrum by comparison to the inelastic signal applying Poisson statistics (Egerton, 1996).

The HAADF study indicates that the La and Ca distribution in the reduced samples is equivalent to the one observed in the starting material previously reported, i.e., Ca is always at the RS layer while the La and Ca randomly occupy the A site at the P block. As representative example, figure S8 shows a HAADF imagecorresponding to $La_{0.5}Ca_{2.5}Mn_2O_{6.5}$ along $[0\ \bar{1}\ 1]_o$. Atomically resolved columns corresponding to La (Z=57), Ca (Z=20) and Mn (Z=25) arranged in an ordered intergrowth between two P and one RS blocks are observed. The brightest dots should be related to a preferential occupation of the heaviest cation, i.e., La, while the less intense to Ca. Provided that the RS blocks exhibit the less brightness, Ca must occupy these sites. Contrarily, the A sites of the P blocks seem to be preferentially occupied by La, according to the brightest contrast of this site. Nevertheless, dots of

less brightness can be also observed suggesting a random occupation La/Ca at the P block. To confirm this situation, atomically resolved maps have been obtained. To enable simultaneous analysis of Ca–$L_{2,3}$ (346 eV), Mn–$L_{2,3}$ (640 eV) and La–$M_{4,5}$ (832 eV) signals, a spectrum imaging (60 x 30 spectra) was recorded by using a dispersion of 0.5 eV per channel. The sum spectra obtained over the area marked in figure S8a, 2.53 nm x 1.27 nm, is depicted in figure S8b. The HAADF image recorded simultaneously to EELS acquisition is depicted in figure S8c. The chemical maps were obtained by analysing every individual spectra of the Ca–$L_{2,3}$ (346-371 eV), Mn–$L_{2,3}$ (640-680 eV) and La–$M_{4,5}$ (832-872 eV) signals. Figure S8d-f shows La, Ca and Mn compositional maps, respectively. These chemical maps indicate that Mn is always located at the B site of the perovskite lattice, La is always placed at the A site of this block, while Ca is at the RS block but also at the P block randomly alternating with La.
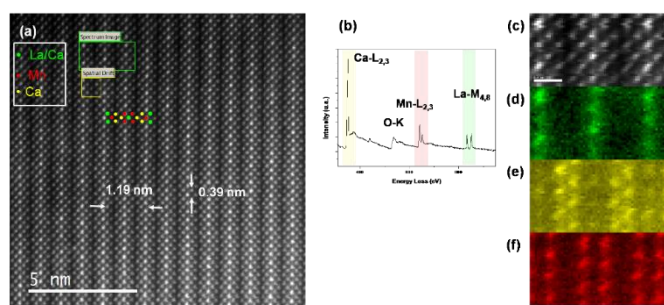

Figure S8 (a) HAADF image along [0$\bar{1}$1]o. A schematic model for the cationic position has been included; (b) EELS spectra sum acquired over the area marked in (a) show the Ca-$L_{2,3}$, O-K, Mn-$L_{2,3}$ and La-M-$_{4,5}$ edges. (c) HAADF image of the region of interest recorded at the same time as the EELS data set acquisition. Chemical maps obtained from La-$M_{4,5}$(d), Ca-$L_{2,3}$ (e), and Mn-$L_{2,3}$ (f) signals.

Using HAADF experimental conditions, the light elements such as oxygen are barely visible, especially when heavy elements are present. On the other hand, using ABF imaging, columns of oxygen atoms have been visualized and clearly distinguished from columns of oxygen vacancies in the $SrMnO_{2.6}$ oxygen deficient perovskite. (Kobayashi *et al*., 2012) This compound exhibits a well-known superstructure as a consequence of the ordering of oxygen deficiency in the MnO_2 layer along [100] and [010] (Suescun *et al*., 2007). In ABF imaging, the collection angle is modified (11-22 mrad) to enhance the contrast of the lighter elements. The required system in the JEOL-JEM ARM200 microscope consists on a bright field detector in which the central area is blanked with a beam stopper providing an annular detector. By modifying the camera length, the appropriate solid angle to enhance the contrast of the oxygen atomic columns is optimized. The resulting image allows the visualization of both light and heavy atomic columns. Acquisition times of 38 s per frame were used for HAADF and ABF images. Figure S9 shows three ABF images characteristic of $La_{0.5}Ca_{2.5}Mn_2O_7$, $La_{0.5}Ca_{2.5}Mn_2O_{6.5}$, $La_{0.5}Ca_{2.5}Mn_2O_{6.25}$. The O sites are visible and no apparent differences are observed

suggesting a randomly O distribution. In the perpendicular direction, characteristic high annular angle dark field (HAADF) and ABF images, simultaneously acquired, are shown in figure 5.
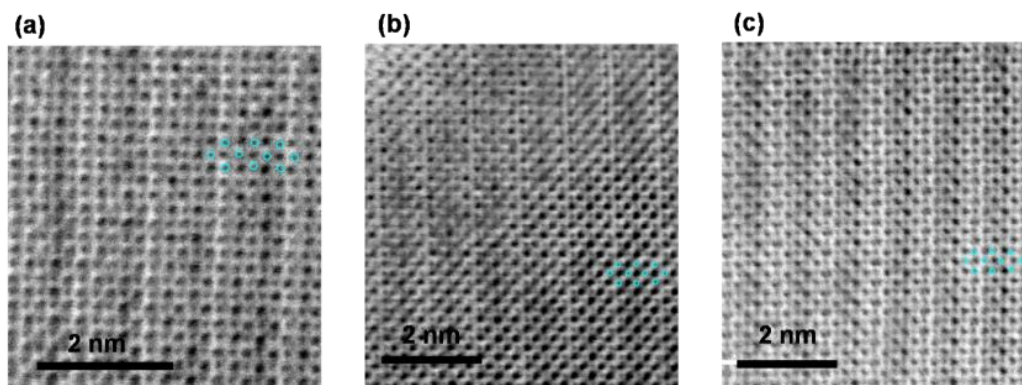

Figure S9   ABF images along $[0\bar{1}1]o$ corresponding to (a) $La_{0.5}Ca_{2.5}Mn_2O_7$, (b) $La_{0.5}Ca_{2.5}Mn_2O_{6.5}$ and (c) $La_{0.5}Ca_{2.5}Mn2O_{6.25}$.
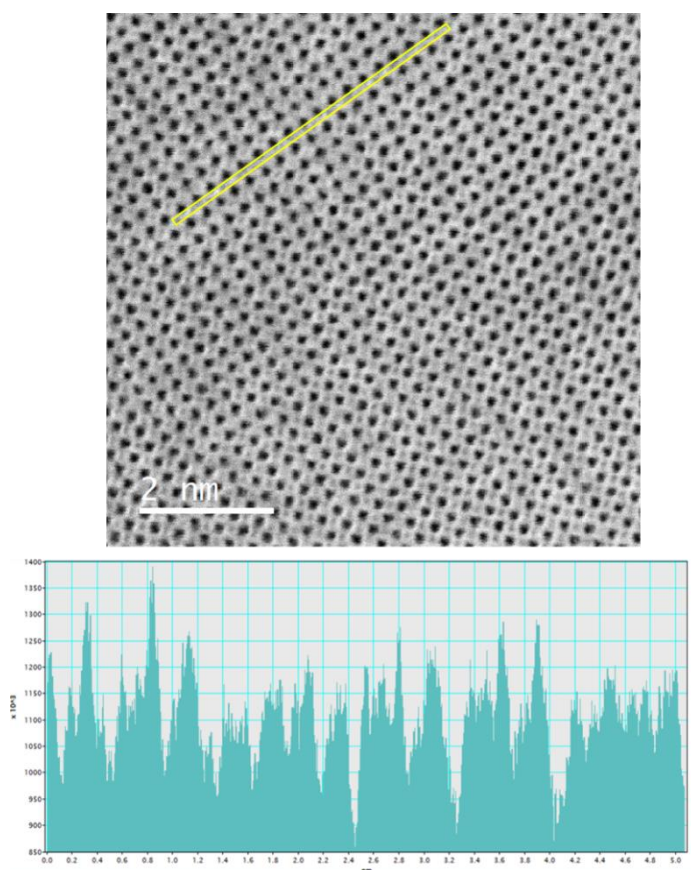

Figure S10 ABF image. An intensity line profile (along the line marked in the image) is shown in the lower part of the image. Intensity changes can be observed.
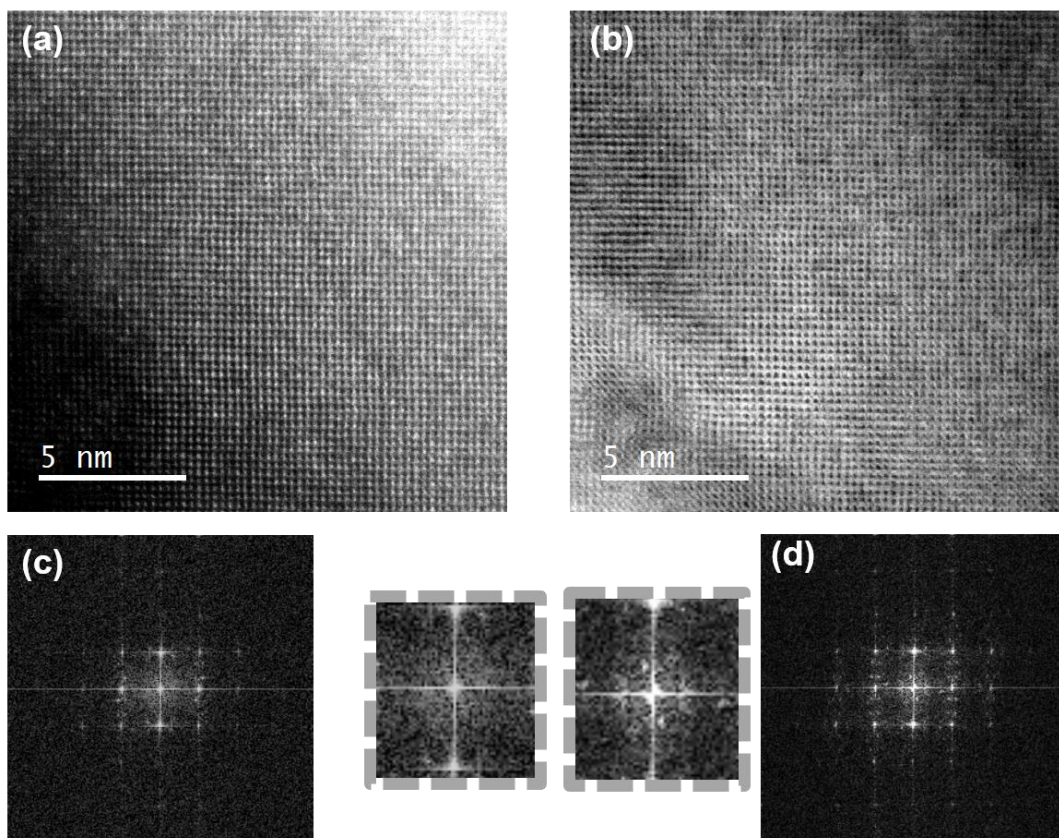
Figure S11. (a) HAADF and (b) ABF low magnification images along $[010]_o$ zone axis. The corresponding FFT are depicted in (c) and (d). It should be notice the clear appearance of superlattice reflections in the FFT obtained from the ABF image (d). These are better observed in the enhanced detail depicted on the left hand side of d) while they are not visible in the FFT obtained from the HAADF image (see (c) and its corresponding enhanced detail place on its right side).

Information concerning the Mn oxidation state has been studied by EELS. For that purpose, the energy dispersion was set to 0.05 eV, in order to increase the energy resolution. Under this condition, punctual analyses corresponding to MnL$_{3,2}$ edge were performed in an average of 50 crystals. Figure S12 shows the representation of the characteristic experimental EELS spectra for the Mn-L$_{3,2}$ edge for the three samples compared, in each case, with well-known standards for Mn^{4+} (Ca$_2$Mn$_3$O$_8$), Mn^{3+} (LaMnO$_3$) and Mn^{2+} (CaMnO$_2$). In the case of La$_{0.5}$Ca$_{2.5}$Mn$_2$O$_7$ (figure S12a), the presence of Mn^{4+} and Mn^{3+} with a higher ratio of the first one, in agreement to the nominal composition (75% Mn^{4+} and 25% of Mn^{3+}), is evident. This ratio is clearly modified for La$_{0.5}$Ca$_{2.5}$Mn$_2$O$_{6.5}$ (figure S12b) since the contribution of Mn^{4+} decreases while Mn^{3+} increases also in agreement with the nominal composition (25% Mn^{4+} and 75% of Mn^{3+}) and the reduction process. Figure S12c shows that for La$_{0.5}$Ca$_{2.5}$Mn$_2$O$_{6.25}$ only Mn^{3+} is present. In order to provide a further insight on the different Mn^{4+} and Mn^{3+}ratio, the relative intensity of the Mn-L$_2$ and Mn-L$_3$ white lines was analyzed. In order to minimize the error due to the spectra background signal, I(L$_3$/L$_2$) values were calculated using the amplitude value obtained from the fitting of the second derivative of the Mn-L$_{2,3}$ white lines to a Gaussian curve (Cortés-Gil *et al.,* 2016; González-Jiménez, *et al.,* 2014). The resulting ratios, in comparison to the standards, are depicted in table S4. From this table, it can be observed that the I(L$_3$/L$_2$) for the most oxidized compound, La$_{0.5}$Ca$_{2.5}$Mn$_2$O$_7$, lies among the standards for Mn^{4+} and Mn^{3+} but closer to Mn^{4+}, in good agreement to the nominal percentages. For La$_{0.5}$Ca$_{2.5}$Mn$_2$O$_{6.5}$, the I(L$_3$/L$_2$) is again between the standards for Mn^{4+} and Mn^{3+} but closer to Mn^{3+}, according to the nominal ratio. A perfect fit with the Mn^{3+} standard is obtained for La$_{0.5}$Ca$_{2.5}$Mn$_2$O$_{6.25}$, where according to the nominal composition only Mn^{3+} is expected.

Table S4   Intensity I (L$_3$/L$_2$) ratio for La$_{0.5}$Ca$_{2.5}$Mn$_2$O$_7$, La$_{0.5}$Ca$_{2.5}$Mn$_2$O$_{6.5}$, La$_{0.5}$Ca$_{2.5}$Mn$_2$O$_{6.25}$ compounds and references for Mn^{4+} (Ca$_2$Mn$_3$O$_8$), Mn^{3+} (LaMnO$_3$) and Mn^{2+} (CaMnO$_2$).

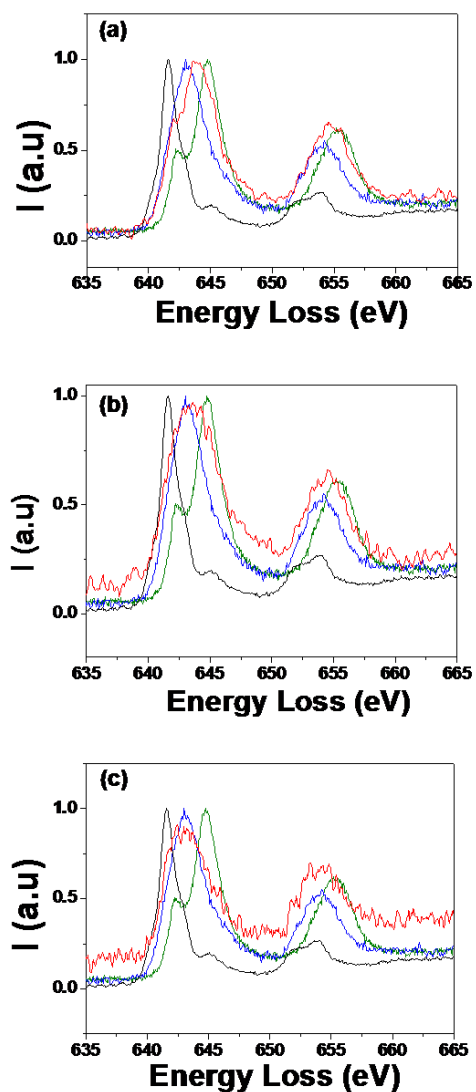| Sample	I (L$_3$/L$_2$)
La$_{0.5}$Ca$_{2.5}$Mn$_2$O$_7$	1.95 ($\pm$0.1)
La$_{0.5}$Ca$_{2.5}$Mn$_2$O$_{6.5}$	2.09 ($\pm$0.1)
La$_{0.5}$Ca$_{2.5}$Mn$_2$O$_{6.2}$	2.4 ($\pm$0.1)
Ca$_2$Mn$_3$O$_8$	1.77 ($\pm$0.1)
LaMnO$_3$	2.43 ($\pm$0.1)
CaMnO$_2$	5.49 ($\pm$0.1)

Figure S12 EELS spectra showing the $L_{2,3}$ Mn edge for (a) $La_{0.5}Ca_{2.5}Mn_2O_7$; (b) $La_{0.5}Ca_{2.5}Mn_2O_{6.5}$; (c) $La_{0.5}Ca_{2.5}Mn_2O_{6.25}$. Spectra corresponding to Mn^{4+} ($Ca_2Mn_3O_8$), Mn^{3+} ($LaMnO_3$) and Mn^{2+} ($CaMnO_2$) are displayed for comparison. Sample spectra are shown in red while standards are marked in green, blue and black for Mn^{4+}, Mn^{3+} and Mn^{2+}, respectively.
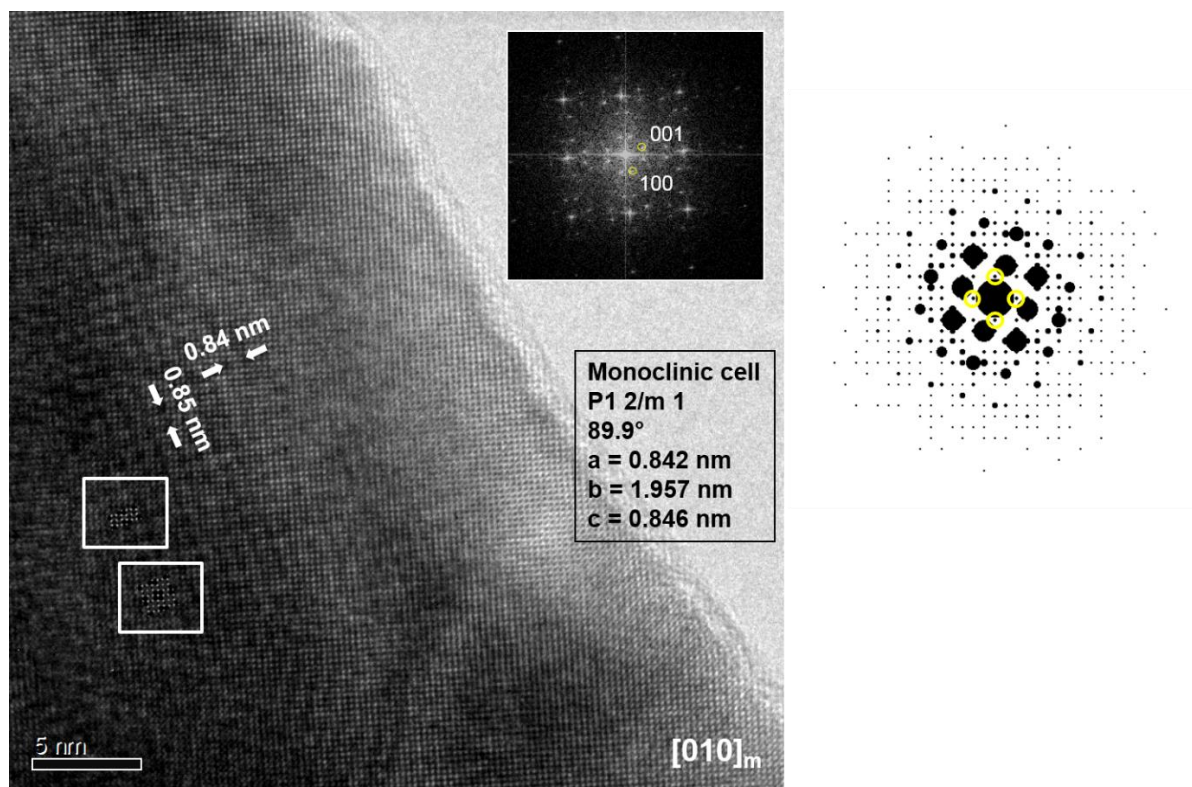
S8. HRTEM image calculation using the structural model resulting from the ND refinement

Figure S13 HREM image shown in figure 3a of the main text. Image calculation for different cells (see the two areas marked in white) having into account the ND refined cell have been inserted. A good agreement between experimental and calculated images is obtained (Δt = 9 nm and Δf=-140 nm). The corresponding calculated SAED has been also included.
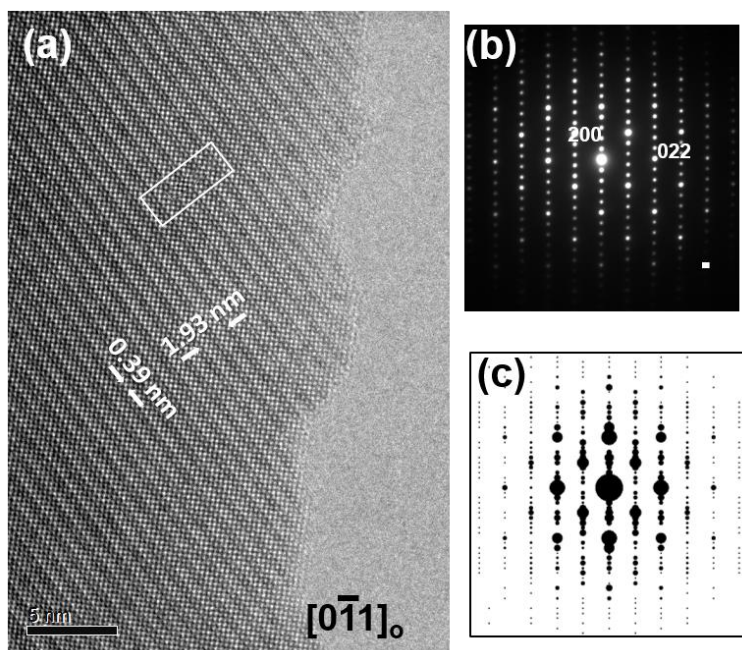
Figure S14 (a) HREM image along $[0\text{-}11]_o$ ($[20\text{-}1]_m$) shown in figure 1c of the main text. Image calculation (marked in white) having into account the ND refined cell has been inserted. A good agreement between experimental and calculated images is obtained ($\Delta t = 2$ nm and $\Delta f = -150$ nm). The corresponding experimental (b) and calculated SAED (c) have been also included.

References

Bendersky, L. A., Cheng, R., Fawcett, I. D. & Greenblatt, M. (2004). *Chem. Mater.* **16**, 5304-5310.

Bonnet, N., Brun, N. & Colliex, C. (1999). *Ultramicroscopy*, **77,** 97-112.

Cortés-Gil, R., Ruiz-González, M. L., González-Merchante, D., Alonso, J. M., Hernando, A., Trasobares, S., Vallet-Regí, M., Rojo J. M. & González-Calbet, J. M. (2016). *Nano Lett.* **16**, 760-765.

Egerton, R. F. (1993). *Electron energy-loss spectroscopy in the electron microscope*, Plenum, New York.

Gillie, L. J., Wright, A. J., Hadermann, J., Van Tendeloo G. & Greaves, C. (2002). *J. Solid State Chem.* **167**, 145-151.

Gillie, L. J., Wright, A. J., Hadermann, J., Van Tendeloo, G. & Greaves, C. (2003). *J. Solid State Chem.* **175**, 188-196.

González-Jiménez, I. N., Torres-Pardo, A., Sánchez-Peláez, A. E., Gutiérrez, A., García-Hernández, M., González-Calbet, J. M., Parras, M. & Varela, A. (2014). *Chem. Mater.* **26**, 2256-2265.

http://hyperspy.org; DOI 10.5281/zenodo.16850.

Kobayashi, S., Findlay, S., Shibata, N., Mizoguchi, T., Sato, Y., Okunishi, E. Ikuhara & Y. Yamamoto, T. (2012). *Appl. Phys. Lett.* **100**, 193112(1-5).

Lee, J. H., Luo, G., Tung, I. C., Chang, S. H., Luo, Z., Malshe, M., Gadre, M., Bhattacharya, A., Nakhmanson, S. M., Eastman, J. A., Hong, H., Jellinek, J., Morgan, D. & Fong, D. D. (2014). *Nature Mater.* **13**, 879-883.

Rijnders, G. (2014). *Nature Mater.* **13**, 844-845.

Ruiz-González, L., González-Merchante, D., Cortés-Gil, R., Alonso, J. M., Martínez, J. L., Hernando, A & González-Calbet, J. M. (2015). *Chem. Mat.* **27**, 1397-1404.

Suescun, L., Chmaissem, O., Mais, J., Dabrowski, B. & Jorgensen, J. D. (2007). *J. Solid State Chem.*, **180**, 1698-1707.

Yan, L., Niu, H., Bridges, C. A., Marshall, P. A., Hadermann, J., Van Tendeloo, G., Chalker, P. R. & Rosseinsky, M. J. (2007). *Angew. Chem., Int. Ed.* **46**, 4539-4542.